Supplementary to Volatile Oxidation Products and Secondary Organosiloxane Aerosol from D_5 + OH at Varying OH Exposures

Hyun Gu Kang[1], Yanfang Chen[2], Jiwoo Jeong[2], Yoojin Park[3], Thomas Berkemeier[1], Hwajin Kim[2,4]

[1]Multiphase Chemistry Department, Max Planck Institute for Chemistry, 55128 Mainz, Germany
[2]Department of Environmental Health Sciences, Graduate School of Public Health, Seoul National University, 08826 Seoul, South Korea
[3]Department of Environmental Science and Engineering, College of Engineering, Ewha Womans University, 03760 Seoul, South Korea
[4]Institute of Health and Environment, Graduate School of Public Health, Seoul National University, 08826 Seoul, South Korea

Correspondence to: Hwajin Kim (khj0116@snu.ac.kr) and Thomas Berkemeier (t.berkemeier@mpic.de)

S1 Experiment and Set Up Details

S1.1 PAM-OFR

Fig. S1 shows the experiment set up. During these experiments, the laboratory room temperatures and pressures were 17 – 21 °C and ~1020 hPa (1 atm) respectively. In this manuscript, we used 1 atm for unit conversions and in KinSim. We passed different flow ratios of dry and humid zero air through the passivated 15 mL glass bulb to get the desired experiment humidity conditions. Mass flow controllers (MFC, MC and MCS series, Alicat Scientific, Tucson, AZ, USA) controlled the input air flow rates. Air coming out of the PAM-OFR and instrument outlets went to the exhaust or through scrubbers to minimize O_3 and aerosol exposure in the room. Ultra-high purity N_2 from a gas cylinder (Sinyang Oxygen Company, Seoul, South Korea) regulated to 30 psig purged the UV lamps.

The PAM-OFR was connected to an O_3 monitor (Model UV-100, 2B Technologies, Boulder, CO, USA) via the outlet side port. For the 120 s τ_{res} experiment, a pump was attached to the outlet side port for additional flow. The PTR-MS inlet and the aerosol sampling line was connected at the OFR outlet center port (Fig. S1). We used perfluoroalkoxy alkane (PFA) tubing (6.35 mm (1/4”) OD, 4.35 mm ID, Sungjin Rubber Industrial, Seoul, South Korea) for the connections to the OFR inlet. The OFR was equipped with conductive Teflon flow rings at both the inlet and the outlet side ports, and the D_5 and humid air were injected through the inlet side port.

We used D_5 (97 %, CAS#541-02-6, Sigma-Aldrich, Saint Louis, MO, USA) as the VOC precursor and stored the D_5 in a refrigerator (~1 °C) when not in use. A syringe pump (Fusion 4000, Chemyx, Stafford, TX, USA) equipped with a 10 uL gas-tight microliter syringe (Model 1801, Hamilton, Reno, NV, USA) continuously injected D_5 into the PAM-OFR. The syringe fed into the passivated glass bulb through a polytetrafluoroethylene-faced (PTFE) septa (13 mm, Scilab, Seoul, South Korea) at room temperature. At the injection speeds and air flow rates used, we did not visually observe any D_5 build-up in the bulb.

For cleaning, making atomizer solutions, and generating humid air for the PAM-OFR, we used Type 1 deionized water (DI water, >18.2 MΩ cm resistivity at 25 °C) from a purification system (Milli-Q Direct 16, Merck, Darmstadt, Germany). We rinsed the microliter syringe between experiments with acetone and DI water and dried them at room temperature in the fume hood. The passivated glass bulb was also rinsed with acetone and DI water and heated in a drying oven before the experiments.

Zero air came from a generator (Model 8301P, Acoem Ecotech, Victoria, Australia) coupled with a catalytic converter set to 520 °C (Model HTO-1000HC, Acoem Ecotech, Victoria, Australia). The zero air also passed through scrubbers filled with activated molecular sieves (4 Å 4 – 8 mesh, Sigma-Aldrich, Saint Louis, MO, USA), $NaMnO_4$ oxidizing media (Purafil SP, Purafil, Doraville, GA, USA), and activated carbon (Purakol, Purafil, Doraville, GA, USA). Lastly, the zero air went through a filtered air supply (Model 3074B, TSI, Shoreview, MN, USA) prior to injection to the PAM-OFR and the Nafion humidifier (FC-100-80-6MKK, Perma Pure, Lakewood, NJ, USA).

To assess the OH_{exp} range, we conducted an offline calibration on the PAM-OFR with calibration CO gas (UnionGas, Gyeonggi-do, South Korea) with a Serinus 30i CO analyzer (Acoem Ecotech, Victoria, Australia). We used humidity conditions close to that of the experiments (Fig. S2). We used the D_5 siloxane trace as a direct measure of OH_{exp} during the experiments themselves and found the OH_{exp} assessed with D_5 to be consistent with the offline calibration with CO. We did not operate the CO analyzer during the experiments to avoid the risk of siloxanes fouling its catalytic converter (Dewil et al., 2006).

S1.2 Aerosol Sampling Line

The aerosol sampling line was connected at the PAM-OFR center outlet port and lead to the SMPS. The sampling line consisted of a O_3 denuder and a Nafion dryer (PD-200T-12MSS, Perma Pure, Lakewood, NJ, USA) with conductive connections and fittings in between. We installed the O_3 denuder in the sampling line to prevent O_3 damage to the SMPS, and it was a diffusion denuder filled with hopcalite pellets (3 mm, Purelyst MD-101, Pure Sphere, Chungcheongnam-do, South Korea). The custom-made diffusion denuder was cylindrical in shape at 52 cm long and 6.5 cm in diameter, and the wet particles would pass through a 12.7 mm (1/2”) ID center line made of stainless mesh. Prior to experiments, we passed filtered compressed air through the O_3 denuder at 10 L min^{-1} for ~30 min to remove any loose particles.

We assessed the O_3 removal by comparing the concentrations entering and exiting the O_3 denuder filled with fresh hopcalite pellets. The flow rate through the O_3 denuder matched that of experiments (3.0 L min^{-1}), and we used the same O_3 monitor used on the PAM-OFR. To generate O_3, humid air was fed into the OFR with 185 nm lights on without siloxanes or seed, and the OFR outputted 2.1 ppm of O_3. We found that the denuder would remove ~90 % of the O_3 by concentration at these test conditions.

We used the particle loss calculator (von der Weiden et al., 2009) with the dimensions of the aerosol sampling line to calculate the size dependent losses in the line (Fig. S3). Given that we did not know at what point when the SOSiA was formed in the PAM-OFR, we only applied the particle loss in the aerosol sampling line to correct the Y_{SOSiA}. The particle loss corrections to the Y_{SOSiA} were done by applying the particle loss at the experiment SOSiA volume mode with that from the calculator.

To prevent siloxane contamination from conductive silicone tubing (Timko et al., 2009; Yu et al., 2009; Asbach et al., 2016), we used conductive PFA tubing (6.35 mm (1/4") OD, 4.76 mm (3/16") ID, Fluorotherm Polymers, Parsippany, NJ, USA) and stainless-steel compression fittings for the connections in the aerosol sampling line. In this experiment set up, we only used conductive silicone tubing (12 cm, 9.53 mm (0.375") OD, 4.8 mm (0.19") ID, TSI, Shoreview, MN, USA) at the inlet of the SMPS and for connections between the SMPS components.

S1.3 Condensational Sink and Condensation Lifetime

We followed the instructions in Section 3.3 of Palm et al. (2016) to calculate the condensational sink (CS, m^{-2}) and low-volatile organic compound (LVOC) condensation lifetimes (τ_{CS}, s), where we used the particle number size distribution from the SMPS. In Eq. (S1), r is the wet particle radius (m), N is the particle number size distribution (m^{-3} at each particle diameter), and β is the dimensionless Fuchs-Sutugin correction factor (Seinfeld and Pandis, 2006). In Eq. (S2), we used the same gas diffusion coefficient (D_g) used by Palm et al. (2016) of 7×10^{-6} m^2 s^{-1}, which represents LVOC. In Eq. (S3), α is the dimensionless accommodation coefficient that is assumed to be 1 (Liu et al., 2019).

$$CS = \int_0^\infty r\beta(r)N(r)dr = \sum_0^\infty r\beta(r)N(r) \quad \text{(S1)}$$

$$\tau_{CS} = \frac{1}{4\pi \times CS \times D_g} \quad \text{(S2)}$$

$$\beta(r) = \frac{Kn+1}{0.377Kn+1+\frac{4}{3}\alpha^{-1}Kn^2+\frac{4}{3}\alpha^{-1}Kn} \quad \text{(S3)}$$

To obtain β, we calculated the dimensionless Knudsen number (Kn), the mean free path (λ_g, m), and the gas average speed (v_{avg}, m s^{-1}) for LVOC at each r. In Eq. (S6), T refers to the temperature (K) in the PAM-OFR and R is the gas constant (R = 8.3145 kg m^2 s^{-2} K^{-1} mol^{-1}). Since particles were dried before being detected by the SMPS, we obtained r in Eq. (S1) and (S4) by multiplying the dry particle radius with the growth factor (*GF*), which is the ratio of the wet particle diameter versus when the particle is dry (Fig. S5).

$$Kn = \frac{\lambda_{\mathrm{g}}}{r} \tag{S4}$$

$$\lambda_g = \frac{3D_{\mathrm{g}}}{v_{\mathrm{avg}}} \tag{S5}$$

$$v_{\mathrm{avg}} = \sqrt{\frac{8\mathrm{R}T}{\pi M}} \tag{S6}$$

We found *GF* with Eq. (S7), where κ is the dimensionless hygroscopicity parameter and α_{w} is the dimensionless water activity approximated via α_{w} = RH %/100. For κ, Palm et al. (2016) used a value representing that of SOA (κ = 0.13), but Janechek et al. (2019) found SOSiA to be non-hygroscopic (κ = 0.01). Consequently, we calculated the *CS* for both the LVOC and SOSiA cases, with molecular weights (*M*) of LVOC, 0.200 kg mol^{-1}, and of D_5, 0.370 kg mol^{-1}. The calculated *GF* for both cases are shown in Fig. S5 and Table S3.

$$\kappa = (GF^3 - 1)(1 - \alpha_{\mathrm{w}})\alpha_{\mathrm{w}}^{-1} \tag{S7}$$

The PAM-OFR has an estimated LVOC eddy diffusion wall loss lifetime (τ_{wall}) of 400 s (Palm et al., 2016), while the calculated τ_{CS} ranged up to ~2 s when using the particle size distribution measured during experiments (Table S3). Palm et al. (2016) recommended using the average of the particle size distributions entering and exiting the OFR, which would double the aforementioned τ_{CS} since we did not use seed aerosol. Either case, we expected the loss of LVOC to the walls to had been small since $\tau_{CS} << \tau_{\mathrm{wall}}$.

S1.4 PTR-MS Inlet and Settings

The PTR-MS inlet was made of SilcoNert 2000-coated (SilcoTek, Bellefonte, PA, USA) stainless steel inlet tubing (1.59 mm (1/16”) OD, 1.0 mm (0.040”) ID) at 1.2 m in length. The PTR-MS was connected immediately at the center outlet of the OFR with SilcoNert 2000-coated fittings (Swagelok, Solon, OH, USA) and conductive PFA tubing (Fluorotherm Polymers, Parsippany, NJ, USA). We set the flow rate into the PTR-MS inlet to 0.43 L min^{-1} using its built-in inlet flow controller and inlet pressure controller. The PTR-MS inlet was equipped with a heating hose set to 60 °C and a dust filter to prevent clogging, especially at the high SOSiA masses. The single stage filter holder was made of PFA (Savillex, Eden Prairie, MN, USA) and held a 25 mm PTFE filter (5 µm pore, Synspec, Groningen, Netherlands) that was replaced daily.

The mass spectrometer extraction time and maximum flight times were 2.0 and 20.0 µs respectively, with the maximum mass at *m/z* 632.0. The mass spectra were integrated and recorded every 1000 ms. For the PTR-MS mass scale calibration, we used $(H_2{}^{18}O)H^+$ (*m/z* 21.0221), $(H_2O)_2H^+$ (*m/z* 37.0284), $(C_6H_4I)H^+$ (*m/z* 203.9431), and $(C_6H_4I_2)H^+$ (*m/z* 330.8475) during the data analysis. We used ioniTOF 4.0 to control the instrument and PTR-MS Viewer 3.4.4 (Ionicon Analytik, Innsbruck, Austria) to process the PTR-MS mass spectra.

S1.5 PTR-MS Mass Spectra Interpretation

D_5 has isotopologues (Fig. 1) whose ion masses overlap with those of VOP. Additionally, large alcohols fragment during the PTR (Brown et al., 2010), and the reported siloxanol (D_4T-OH) or siloxanediol (D_3T_2-(OH)$_2$) may have fragmented if they behave like saturated organic alcohols. Since we did not have siloxanol calibration standards, we opted to use the -OH fragmentation behavior of organic alcohols to assess the qualitative trends of the proposed VOP.

We used the -OH fragment of D_4T-OH at *m/z* 355, the -OH fragment of D_3T_2-(OH)$_2$ at *m/z* 357, and the -OH fragment of D_3T_2-OH-OCHO at *m/z* 385 to assess the relative trends of these VOP (Table S4). However, the signal at *m/z* 355 overlaps with the -CH_3 fragment of D_5 ($C_9H_{27}O_5Si_5{}^+$), as noted by Coggon et al. (2018). As for *m/z* 357, this signal overlaps with an isotopologue of the -CH_3 fragment of D_5 and the -OH fragment of D_4T-OH. To retrieve the signal of D_4T-OH and D_3T_2-(OH)$_2$, we subtracted the fragment and/or isotopologue signals from the total signal at the designated ion masses. For *m/z* 355, we subtracted the -CH_3 fragment of D_5 using the 355/371 ratio of D_5 found prior to the experiment. For *m/z* 357, we subtracted the $C_9H_{27}O_5Si_5{}^+$ isotopologue signal fraction.

For the quantification of D_5, we opted to use the main D_5 ion $(C_{10}H_{30}Si_5)H^+$ at *m/z* 371, as opposed to the -CH_3 fragment ion at *m/z* 355. Coggon et al. (2018) used the D_5 fragment ion for their ambient air measurements due to higher ion counts there. $C_9H_{27}O_5Si_5{}^+$ had a higher ion count than $(C_{10}H_{30}Si_5)H^+$ during our calibrations and experiments as well, but the D_5 concentrations in these experiments were sufficiently high for quantification at *m/z* 371. Additionally, Since the -OH fragment ion of D_4T-OH has the same elemental composition of the -CH_3 fragment of D_5, we chose the *m/z* 371 D_5 ion to avoid potential overlaps in the D_5 quantification.

The PTR-MS is limited in the species it can detect and resolve. The PTR-MS configuration restricts the volatility range of identifiable species, where species are not fragmented during the PTR or lost on the surfaces of the instrument and inlet. Moreover, the PTR is known to fragment peroxides (Li et al., 2022), which limits their detection. Saturated alcohols larger than ethanol and unsaturated alcohols are also known to undergo fragmentation during ionization in the PTR-MS (Brown et al., 2010; Demarcke et al., 2010). Consequently, we cannot rule out that some D_5 VOP fragments are being misattributed in the trends that we report.

For example, methanediol ($CH_2(OH)_2$) is the hydrated form of HCHO and has been observed to largely fragment to a $-H_2O$ PTR ion that overlaps at *m/z* 31 (Franco et al., 2021). Although $CH_2(OH)_2$ may be formed in the gas phase through HCHO + H_2O via HCOOH catalysis (Hazra et al., 2013), the gaseous compound is thought to have evaporated after forming heterogeneously (Franco et al., 2021). Franco et al. (2021) also fitted the gaseous unimolecular dehydration ($CH_2(OH)_2 \rightarrow HCHO + H_2O$) rate coefficient $k_{CH2(OH)2}$ to be 8.5×10^{-5} s^{-1}, which gives the species a unimolecular dehydration lifetime of 0.14 days, which is longer than the residence time of the PAM-OFR. The dominant products from $CH_2(OH)_2$ + OH are HCOOH and HO_2 via the decomposition of the RO_2, and so this diol is practically an intermediate between HCHO and HCOOH.

Given the humid PAM-OFR conditions, $CH_2(OH)_2$ may have been present, and the -OH fragment ion may have led to the over-quantification of HCHO; the fragmentation of $CH_2(OH)_2$ during the PTR needs to be characterized to constrain this uncertainty. However, Franco et al. (2021) found that $CH_2(OH)_2$ + OH has a rate coefficient of $k_{CH2(OH)2+OH}$ = ~7.5×10^{-12} cm^3 s^{-1}, and so we expected $CH_2(OH)_2$ to have a OH-oxidation lifetime less than that of τ_{res} at the [OH] in the PAM-OFR. Consequently, we did not expect the $CH_2(OH)_2$ -OH fragment interference to the HCHO quantification to be large.

S2 SOSiA Mass Density (ρ_{SOSiA})

In a separate series of experiments, we collected SOSiA filter samples from the PAM-OFR on pre-weighed PTFE filters (47 mm, 2 μm pore, PT48P-KR, MTL, Minneapolis, MN, USA), where we also operated the SMPS. Then, we stored the filter samples in a desiccator placed inside of a temperature and humidity-controlled micro-balance room for a day. We used a semi-micro balance (± 0.1 mg, ME204, Mettler Toledo, Columbus, OH, USA) to weigh the filters and calculated the mean ρ_{SOSiA} by dividing the masses of SOSiA collected over integrated SMPS volumes.

From five filter samples, we found a mean (± standard error) ρ_{SOSiA} of 1.07 ± 0.04 g cm^{-3}. We note that existing publications used discrepant ρ_{SOSiA} values, which are summarized in Table S9. That range includes those representing SOA (Charan et al., 2022) or D_5 itself (Janechek et al., 2019). Wu and Johnston (2017) did not explicitly state the ρ_{SOSiA} they used. Han et al. (2022) used particle size and mass data from an SMPS and an AMS to get ρ_{SOSiA} of 1.6 – 1.8 g cm^{-3} for SOSiA from different siloxane precursors. Avery et al. (2023) used the SOSiA elemental ratios from the AMS with the method described by Kuwata et al. (2012) to obtain ρ_{SOSiA} of 1.59 – 1.78 g cm^{-3}.

For reference, Fytas and Wang (1984) measured the density of several methylphenylsiloxane oligomers, which ranged from 0.99 – 1.10 g cm^{-3}, while He et al. (1988) used a polydimethylsiloxane density parameterization based on molecular weight that maximizes to 0.97 g cm^{-3}. Dee et al. (1992) measured the densities of polydimethylsiloxane oligomers and found values between 1 to 1.14 g cm^{-3}. One of the silanols formed in the siloxane degradation process is dimethylsilanediol (DMSD,

$C_2H_8O_2Si$), and Mazzoni et al. (1997) calculated DMSD to have a density of 1.023 g cm^{-3} at 20 °C using a group contribution method. Lamers et al. (2021) found that dimethylsiloxane oligomers of varying lengths would have densities of ~1 g cm^{-3}.

While the ρ_{SOSiA} we measured are in line with literature siloxane/silanol densities, they are lower than those reported by Han et al. (2022) and Avery et al. (2023). Some of the difference between their and our ρ_{SOSiA} measurements may be explained by the different experiment conditions, such as OH_{exp}, since aerosol density is expected to increase with higher oxygenation (Kuwata et al., 2012; Nakao et al., 2013). Moreover, Han et al. (2022), Avery et al. (2023), and this study each used different methods to measure ρ_{SOSiA}.

S3 PTR-MS Calibration

For HCHO, we used a paraformaldehyde permeation tube (CAS#30525-89-4, VICI Metronics, Poulsbo, WA, USA) and a calibration gas generator (Model 150 Dynacalibrator, VICI Metronics, Poulsbo, WA, USA) set to 70 °C to produce HCHO calibration gas with ultra-high purity N_2 as the carrier gas. To achieve a steady output, we conditioned the permeation tube in the calibration gas generator for a week at the temperature and carrier gas flow rate to be used during the calibration. The HCHO calibration gas was diluted dynamically to achieve target concentrations with zero/humid air and MFCs, and we corrected the HCHO quantification for humidity using Eq. (S8) from Vlasenko et al. (2010), where k_{rev} is the fitted reverse PTR rate coefficient (cm^3 s^{-1}), $[H_2O]_{dry}$ is the H_2O concentration (cm^{-3}) in the drift tube when sample air is dry, $[H_2O]$ is the water concentration (cm^{-3}) in the drift tube when sample air is humid, and Δt is the drift tube reaction time (9.4×10^{-5} s).

$$\frac{\text{Sensitivity}_{\text{meas}}}{\text{Sensitivity}_{\text{dry}}} = \frac{[H_2O]_{\text{dry}}\left(1-e^{-k_{\text{rev}}[H_2O]\Delta t}\right)}{[H_2O]\left(1-e^{-k_{\text{rev}}[H_2O]_{\text{dry}}\Delta t}\right)} \quad \text{(S8)}$$

To obtain $[H_2O]_{dry}$, we followed the method described in Vlasenko et al. (2010), where we fitted a quadratic polynomial (Eq. (S9)) to $(H_2O)_2H^+$ (ncps) against the sample air absolute humidity (Fig. S6.B3). Then, we took the fitted y-intercept (≈ 4000) and linearly approximated the corresponding absolute humidity at 2×y-intercept, which comes to be ~0.005 mol/mol. Lastly, we converted the $[H_2O]_{dry}$ mixing ratio to cm^{-3} using the drift tube pressure (2.30 mbar) and temperature (80 °C).

$$I_{(H2O)2H+} = A + Bx + Cx^2 \quad \text{(S9)}$$

For HCOOH, a 1 % (w/w) aqueous solution of HCOOH (>98.0 %, CAS#64-18-6, Tokyo Chemical Industry, Tokyo, Japan) was injected into the VOC bulb with a syringe pump and zero/humid air flowing through the bulb. Like Baasandorj et al. (2015), we found the PTR-MS sensitivity at *m/z* 47 to be affected by humidity, with sensitivity decreasing with higher RH at

137 Td. Consequently, we adjusted the HCOOH quantification for H_2O cluster effects with the method outlined in Baasandorj et al. (2015). We fitted the parameters in Eq. (S10), where x is $I_{(H2O)2H+}/I_{(H2O)H+}$.

$$\text{Sensitivity} = A \times \left(B_1 exp(C_1 x) + B_2 exp(C_2 x)\right) \quad \text{(S10)}$$

S4 Odum 2-product Model

Eq. (S11) shows the Odum 2-product parameterization (Odum et al., 1996) for aerosol mass yields, in this case for SOSiA. Janechek et al. (2019) and Charan et al. (2022) fitted their data, and we also parameterize the experimental Y_{SOSiA} with the 2-product model in Eq. (S11) for comparison. The partitioning coefficient (K, m^3 µg^{-1}) is the inverse of the saturation mass concentration C^* (µg m^{-3}), C_{OA} is the OA mass loading (µg m^{-3}), and α is the product yield for each corresponding K. The fitted values and the literature comparison is shown in Fig. S7, and the Y_{SOSiA} have been adjusted for ρ_{SOSiA} = 1.07 g cm^{-3}.

$$Y_{\text{SOSiA}} = C_{\text{OA}} \left(\frac{\alpha_1 K_1}{1+K_1 C_{\text{OA}}} + \frac{\alpha_2 K_2}{1+K_2 C_{\text{OA}}}\right) \quad \text{(S11)}$$

We fit the 2-product model with the ρ_{SOSiA}-adjusted data from Han et al. (2022), Avery et al. (2023), and all literature values combined, including those we report. The existing literature values and fit 2-product model parameters are summarized in Tables S9 and S10. As shown in Fig. 4, the 2-product model parameters provided by Charan et al. (2022) are consistent with those of Han et al. (2022) and Avery et al. (2023) at ambient surface C_{OA} (0-30 µg m^{-3}) with low Y_{SOSiA}. However, the 2-product model fit of Janechek et al. (2019) predicts less volatile products, resulting in higher Y_{SOSiA} at those C_{OA}. Our 2-product model fit predicts more volatile products, which is consistent with that of Charan et al. (2022), Han et al. (2022), and Avery et al. (2023).

However, for the high C_{OA} cases, the literature diverges with experimental Y_{SOSiA} ranging from 10 to 100 % at ~200 µg m^{-3}, and our Y_{SOSiA} yield curve lies between the curves from the literature (Fig. S7). The intercorrelation of OH_{exp} with Y_{SOSiA} is also visible in Fig. S7, where the higher Y_{SOSiA} measurements occur not only when C_{OA} is high, but also as OH_{exp} increases (color scale). The 2-product model here does not explicitly account for chemical aging with OH_{exp}, so we use the aging-VBS approach.

S5 Modeling RO_2 Pathways with KinSim

A potential explanation for the Y_{SOSiA} discrepancies in the literature is the RO_2 fate, where high [OH] in OFR experiments may have pushed the RO_2 fate towards a pathway that forms more condensing species. However, Alton and Browne (2022) found in their chamber that $RO_2 + HO_2$, RO_2 + NO, and unimolecular pathways would yield similar fractions of siloxanol and formate ester, suggesting these pathways make similar products, likely through RO; Alton and Browne (2022) suggests that the dominant products of $RO_2 + HO_2$ are RO, OH, and O_2, instead of ROOH.

In OFR185, the RO_2 + OH pathway is feasible due to high [OH] and the atmospheric relevance of this pathway is debated (Peng and Jimenez, 2020). However, Fittschen (2019) suggests that RO_2 + OH is an atmospherically-relevant pathway in low-NO_x environments, and the dominant product is expected to be RO (+ HO_2). That being said, Assaf et al. (2018) found that the dominant product of RO_2 + OH is ROOOH for RO_2 with more than 3 carbon atoms, but we are unaware of any documentation of siloxane RO_2 forming ROOOH. The dominance of RO products across RO_2 fates leading to comparable aerosol mass yields has been reported with monoterpene nitrate oxidation as well (Day et al., 2022).

To assess the RO_2 fates in these experiments, we adopted analogous reactions from the literature and added those RO_2 fates into an OFR mechanism template (Peng and Jimenez, 2020) for KinSim 4.16, a chemical kinetics simulator (Peng and Jimenez, 2019). Table S5 shows the additional RO_2 reactions and rate coefficients appended to the OFR mechanism. The results suggest that $RO_2 + HO_2$ and RO_2 + OH pathways dominated across the experiments, but we encountered an issue reconciling the measured OH_{exp} using Eq. (2) and the OH_{exp} from KinSim.

To input the 254 and 185 nm photon fluxes (I_{254} and I_{185}) in KinSim, we followed the recommendations in Rowe et al. (2020) with $I_{254max} = 3.0 \times 10^{15}$ cm^{-2} s^{-1} and I_{185max}:I_{254max} = 0.0664. Next, we multiplied I_{254max} and I_{185max} by 0.1 to account for the shrink wrap lamp covers and by the ratios of the experiment irradiance and O_3 outputs versus the maximum values at 8V (Table S6). However, we found that with the above photon flux inputs, KinSim calculated the OH_{exp} to be too high and $[D_5]_{final}$ to be too low, although the modeled [O_3] were consistent with measurements (Fig. S9).

Given that we were interested in probing the RO_2 fates, we multiplied I_{185} and I_{254} by a factor of 0.1 to bring the OH_{exp} and $[D_5]_{final}$ in line with measurements. We used I_{185} of $3 \times 10^{11} – 2 \times 10^{12}$ and I_{254} of $1 \times 10^{12} – 3 \times 10^{13}$ cm^{-2} s^{-1} in the case where I_{185} and I_{254} are multiplied by a factor of 0.1, and the initial fluxes are summarized in Table S6. However, this adjustment led to the output [O_3] being underestimated. To assess the impact of the adjustment on RO_2 fates, we modelled both cases where I_{185} and I_{254} are and are not adjusted (Fig. S10).

In both UV flux cases, KinSim found $RO_2 + HO_2$ and RO_2 + OH to be the dominant reaction pathways across the experiments (Fig. S10). A potential explanation for the OH_{exp} discrepancy is the formation of secondary products that are also reactive with OH, which are not included in OHR_{ext} calculated with injected D_5. Since we observed the formation of OH-reactive species like HCHO and the proposed VOP appear to be removed with OH_{exp}, we suspect that the KinSim mechanism is incomplete, and that a more complete mechanism with subsequent OH-reactive species should improve the KinSim calculations.

For these experiments, we expected RO_2 + HO_2 and RO_2 + OH to have been the dominant pathways across the experiments, based on the findings by Alton and Browne (2022) and the KinSim calculations. Avery et al. (2023) also found similar RO_2 fates with KinSim for their experiments, and the common product of these pathways is RO. We note that the inclusion of VOP into the OFR mechanism or when calculating OHR_{ext} may be needed to reconcile measured OH_{exp} and model expectations. Peng and Jimenez (2020) suggest that using measured OH_{exp} is preferred over modelled values due to uncertainties in the OFR residence time, mixing, and OH recycling. We also used RO_2 reactions and rate coefficients in the OFR mechanism based on those of organics, and that the RO_2 fates are subject to change as the D_5 + OH system is further constrained.

References

Alton, M. W. and Browne, E. C.: Atmospheric Chemistry of Volatile Methyl Siloxanes: Kinetics and Products of Oxidation by OH Radicals and Cl Atoms, Environ Sci Technol, 54, 5992–5999, https://doi.org/10.1021/acs.est.0c01368, 2020.

Alton, M. W. and Browne, E. C.: Atmospheric Degradation of Cyclic Volatile Methyl Siloxanes: Radical Chemistry and Oxidation Products, ACS Environmental Au, https://doi.org/10.1021/acsenvironau.1c00043, 2022.

Asbach, C., Kaminski, H., Lamboy, Y., Schneiderwind, U., Fierz, M., and Todea, A. M.: Silicone sampling tubes can cause drastic artifacts in measurements with aerosol instrumentation based on unipolar diffusion charging, Aerosol Science and Technology, 50, 1375–1384, https://doi.org/10.1080/02786826.2016.1241858, 2016.

Assaf, E., Schoemaecker, C., Vereecken, L., and Fittschen, C.: Experimental and theoretical investigation of the reaction of RO2 radicals with OH radicals: Dependence of the HO2 yield on the size of the alkyl group, Int J Chem Kinet, 50, 670–680, https://doi.org/https://doi.org/10.1002/kin.21191, 2018.

Atkinson, R.: Kinetics of the gas-phase reactions of a series of organosilicon compounds with hydroxyl and nitrate(NO3) radicals and ozone at 297 +- 2 K, Environ Sci Technol, 25, 863–866, https://doi.org/10.1021/es00017a005, 1991.

Atkinson, R., Baulch, D. L., Cox, R. A., Crowley, J. N., Hampson, R. F., Hynes, R. G., Jenkin, M. E., Rossi, M. J., Troe, J., and Subcommittee, I.: Evaluated kinetic and photochemical data for atmospheric chemistry: Volume II – gas phase reactions of organic species, Atmos Chem Phys, 6, 3625–4055, https://doi.org/10.5194/acp-6-3625-2006, 2006.

Avery, A. M., Alton, M. W., Canagaratna, M. R., Krechmer, J. E., Sueper, D. T., Bhattacharyya, N., Hildebrandt Ruiz, L., Brune, W. H., and Lambe, A. T.: Comparison of the Yield and Chemical Composition of Secondary Organic Aerosol

Generated from the OH and Cl Oxidation of Decamethylcyclopentasiloxane, ACS Earth Space Chem, https://doi.org/10.1021/acsearthspacechem.2c00304, 2023.

Baasandorj, M., Millet, D. B., Hu, L., Mitroo, D., and Williams, B. J.: Measuring acetic and formic acid by proton-transfer-reaction mass spectrometry: sensitivity, humidity dependence, and quantifying interferences, Atmos Meas Tech, 8, 1303–1321, https://doi.org/10.5194/amt-8-1303-2015, 2015.

Brown, P., Watts, P., Märk, T. D., and Mayhew, C. A.: Proton transfer reaction mass spectrometry investigations on the effects of reduced electric field and reagent ion internal energy on product ion branching ratios for a series of saturated alcohols, Int J Mass Spectrom, 294, 103–111, https://doi.org/https://doi.org/10.1016/j.ijms.2010.05.028, 2010.

Charan, S. M., Huang, Y., Buenconsejo, R. S., Li, Q., Cocker III, D. R., and Seinfeld, J. H.: Secondary organic aerosol formation from the oxidation of decamethylcyclopentasiloxane at atmospherically relevant OH concentrations, Atmos Chem Phys, 22, 917–928, https://doi.org/10.5194/acp-22-917-2022, 2022.

Coggon, M. M., McDonald, B. C., Vlasenko, A., Veres, P. R., Bernard, F., Koss, A. R., Yuan, B., Gilman, J. B., Peischl, J., Aikin, K. C., DuRant, J., Warneke, C., Li, S.-M., and de Gouw, J. A.: Diurnal Variability and Emission Pattern of Decamethylcyclopentasiloxane (D5) from the Application of Personal Care Products in Two North American Cities, Environ Sci Technol, 52, 5610–5618, https://doi.org/10.1021/acs.est.8b00506, 2018.

Day, D. A., Fry, J. L., Kang, H. G., Krechmer, J. E., Ayres, B. R., Keehan, N. I., Thompson, S. L., Hu, W., Campuzano-Jost, P., Schroder, J. C., Stark, H., DeVault, M. P., Ziemann, P. J., Zarzana, K. J., Wild, R. J., Dubè, W. P., Brown, S. S., and Jimenez, J. L.: Secondary Organic Aerosol Mass Yields from NO3 Oxidation of α-Pinene and Δ-Carene: Effect of RO2 Radical Fate, J Phys Chem A, 126, 7309–7330, https://doi.org/10.1021/acs.jpca.2c04419, 2022.

Dee, G. T., Ougizawa, T., and Walsh, D. J.: The pressure-volume-temperature properties of polyethylene, poly(dimethyl siloxane), poly(ethylene glycol) and poly(propylene glycol) as a function of molecular weight, Polymer (Guildf), 33, 3462–3469, https://doi.org/https://doi.org/10.1016/0032-3861(92)91104-A, 1992.

Demarcke, M., Amelynck, C., Schoon, N., Dhooghe, F., Rimetz-Planchon, J., van Langenhove, H., and Dewulf, J.: Laboratory studies in support of the detection of biogenic unsaturated alcohols by proton transfer reaction-mass spectrometry, Int J Mass Spectrom, 290, 14–21, https://doi.org/https://doi.org/10.1016/j.ijms.2009.11.005, 2010.

Dewil, R., Appels, L., and Baeyens, J.: Energy use of biogas hampered by the presence of siloxanes, Energy Convers Manag, 47, 1711–1722, https://doi.org/https://doi.org/10.1016/j.enconman.2005.10.016, 2006.

Fittschen, C.: The reaction of peroxy radicals with OH radicals, Chem Phys Lett, 725, 102–108, https://doi.org/https://doi.org/10.1016/j.cplett.2019.04.002, 2019.

Franco, B., Blumenstock, T., Cho, C., Clarisse, L., Clerbaux, C., Coheur, P.-F., de Mazière, M., de Smedt, I., Dorn, H.-P., Emmerichs, T., Fuchs, H., Gkatzelis, G., Griffith, D. W. T., Gromov, S., Hannigan, J. W., Hase, F., Hohaus, T., Jones, N., Kerkweg, A., Kiendler-Scharr, A., Lutsch, E., Mahieu, E., Novelli, A., Ortega, I., Paton-Walsh, C., Pommier, M., Pozzer, A., Reimer, D., Rosanka, S., Sander, R., Schneider, M., Strong, K., Tillmann, R., van Roozendael, M., Vereecken, L., Vigouroux, C., Wahner, A., and Taraborrelli, D.: Ubiquitous atmospheric production of organic acids mediated by cloud droplets, Nature, 593, 233–237, https://doi.org/10.1038/s41586-021-03462-x, 2021.

Fytas, G. and Wang, C. H.: Studies of siloxane oligomers by depolarized Rayleigh scattering, J Am Chem Soc, 106, 4392–4396, https://doi.org/10.1021/ja00328a017, 1984.

Han, C., Yang, H., Li, K., Lee, P., Liggio, J., Leithead, A., and Li, S.-M.: Secondary organic aerosols from OH oxidation of cyclic volatile methyl siloxanes as an important Si source in the atmosphere, Atmos Chem Phys, 22, 10827–10839, https://doi.org/10.5194/acp-22-10827-2022, 2022.

Hazra, M. K., Francisco, J. S., and Sinha, A.: Gas Phase Hydrolysis of Formaldehyde To Form Methanediol: Impact of Formic Acid Catalysis, J Phys Chem A, 117, 11704–11710, https://doi.org/10.1021/jp4008043, 2013.

He, X. W., Widmaier, J. M., Herz, J. E., and Meyer, G. C.: Competition between polycondensation of α,ω-dihydroxy polydimethylsiloxane and its condensation with alkoxy silane: A kinetic approach, Eur Polym J, 24, 1145–1148, https://doi.org/https://doi.org/10.1016/0014-3057(88)90100-0, 1988.

Janechek, N. J., Marek, R. F., Bryngelson, N., Singh, A., Bullard, R. L., Brune, W. H., and Stanier, C. O.: Physical properties of secondary photochemical aerosol from OH oxidation of a cyclic siloxane, Atmos Chem Phys, 19, 1649–1664, https://doi.org/10.5194/acp-19-1649-2019, 2019.

Kim, J. and Xu, S.: Quantitative structure-reactivity relationships of hydroxyl radical rate constants for linear and cyclic volatile methylsiloxanes, Environ Toxicol Chem, 36, 3240–3245, https://doi.org/https://doi.org/10.1002/etc.3914, 2017.

Kuwata, M., Zorn, S. R., and Martin, S. T.: Using Elemental Ratios to Predict the Density of Organic Material Composed of Carbon, Hydrogen, and Oxygen, Environ Sci Technol, 46, 787–794, https://doi.org/10.1021/es202525q, 2012.

Lamers, B. A. G., de Waal, B. F. M., and Meijer, E. W.: The iterative synthesis of discrete dimethylsiloxane oligomers: A practical guide, Journal of Polymer Science, 59, 1142–1150, https://doi.org/https://doi.org/10.1002/pol.20200649, 2021.

Li, H., Almeida, T. G., Luo, Y., Zhao, J., Palm, B. B., Daub, C. D., Huang, W., Mohr, C., Krechmer, J. E., Kurtén, T., and Ehn, M.: Fragmentation inside proton-transfer-reaction-based mass spectrometers limits the detection of ROOR and ROOH peroxides, Atmos Meas Tech, 15, 1811–1827, https://doi.org/10.5194/amt-15-1811-2022, 2022.

Liu, X., Day, D. A., Krechmer, J. E., Brown, W., Peng, Z., Ziemann, P. J., and Jimenez, J. L.: Direct measurements of semi-volatile organic compound dynamics show near-unity mass accommodation coefficients for diverse aerosols, Commun Chem, 2, 98, https://doi.org/10.1038/s42004-019-0200-x, 2019.

Mazzoni, S. M., Roy, S., and Grigoras, S.: Eco-Relevant Properties of Selected Organosilicon Materials, in: Organosilicon Materials, edited by: Chandra, G., Springer Berlin Heidelberg, Berlin, Heidelberg, 53–81, https://doi.org/10.1007/978-3-540-68331-5_3, 1997.

Nakao, S., Tang, P., Tang, X., Clark, C. H., Qi, L., Seo, E., Asa-Awuku, A., and Cocker, D.: Density and elemental ratios of secondary organic aerosol: Application of a density prediction method, Atmos Environ, 68, 273–277, https://doi.org/https://doi.org/10.1016/j.atmosenv.2012.11.006, 2013.

Odum, J. R., Hoffmann, T., Bowman, F., Collins, D., Flagan, R. C., and Seinfeld, J. H.: Gas/Particle Partitioning and Secondary Organic Aerosol Yields, Environ Sci Technol, 30, 2580–2585, https://doi.org/10.1021/es950943+, 1996.

Otkjær, R. V., Jakobsen, H. H., Tram, C. M., and Kjaergaard, H. G.: Calculated Hydrogen Shift Rate Constants in Substituted Alkyl Peroxy Radicals, J Phys Chem A, 122, 8665–8673, https://doi.org/10.1021/acs.jpca.8b06223, 2018.

Palm, B. B., Campuzano-Jost, P., Ortega, A. M., Day, D. A., Kaser, L., Jud, W., Karl, T., Hansel, A., Hunter, J. F., Cross, E. S., Kroll, J. H., Peng, Z., Brune, W. H., and Jimenez, J. L.: In situ secondary organic aerosol formation from ambient pine forest air using an oxidation flow reactor, Atmos Chem Phys, 16, 2943–2970, https://doi.org/10.5194/acp-16-2943-2016, 2016.

Peng, Z. and Jimenez, J. L.: KinSim: A Research-Grade, User-Friendly, Visual Kinetics Simulator for Chemical-Kinetics and Environmental-Chemistry Teaching, J Chem Educ, 96, 806–811, https://doi.org/10.1021/acs.jchemed.9b00033, 2019.

Peng, Z. and Jimenez, J. L.: Radical chemistry in oxidation flow reactors for atmospheric chemistry research, Chem. Soc. Rev., 49, 2570–2616, https://doi.org/10.1039/C9CS00766K, 2020.

Rowe, J. P., Lambe, A. T., and Brune, W. H.: Technical Note: Effect of varying the λ=185 and 254nm photon flux ratio on radical generation in oxidation flow reactors, Atmos Chem Phys, 20, 13417–13424, https://doi.org/10.5194/acp-20-13417-2020, 2020.

Safron, A., Strandell, M., Kierkegaard, A., and Macleod, M.: Rate Constants and Activation Energies for Gas-Phase Reactions of Three Cyclic Volatile Methyl Siloxanes with the Hydroxyl Radical, Int J Chem Kinet, 47, 420–428, https://doi.org/https://doi.org/10.1002/kin.20919, 2015.

Seinfeld, J. H. and Pandis, S. N.: Atmospheric Chemistry and Physics: From Air Pollution to Climate Change, 1203 pp., 2006.

Timko, M. T., Yu, Z., Kroll, J., Jayne, J. T., Worsnop, D. R., Miake-Lye, R. C., Onasch, T. B., Liscinsky, D., Kirchstetter, T. W., Destaillats, H., Holder, A. L., Smith, J. D., and Wilson, K. R.: Sampling Artifacts from Conductive Silicone Tubing, Aerosol Science and Technology, 43, 855–865, https://doi.org/10.1080/02786820902984811, 2009.

Vlasenko, A., Macdonald, A. M., Sjostedt, S. J., and Abbatt, J. P. D.: Formaldehyde measurements by Proton transfer reaction – Mass Spectrometry (PTR-MS): correction for humidity effects, Atmos Meas Tech, 3, 1055–1062, https://doi.org/10.5194/amt-3-1055-2010, 2010.

von der Weiden, S.-L., Drewnick, F., and Borrmann, S.: Particle Loss Calculator – a new software tool for the assessment of the performance of aerosol inlet systems, Atmos Meas Tech, 2, 479–494, https://doi.org/10.5194/amt-2-479-2009, 2009.

Wu, Y. and Johnston, M. V: Aerosol Formation from OH Oxidation of the Volatile Cyclic Methyl Siloxane (cVMS) Decamethylcyclopentasiloxane, Environ Sci Technol, 51, 4445–4451, https://doi.org/10.1021/acs.est.7b00655, 2017.

Xiao, R., Zammit, I., Wei, Z., Hu, W.-P., MacLeod, M., and Spinney, R.: Kinetics and Mechanism of the Oxidation of Cyclic Methylsiloxanes by Hydroxyl Radical in the Gas Phase: An Experimental and Theoretical Study, Environ Sci Technol, 49, 13322–13330, https://doi.org/10.1021/acs.est.5b03744, 2015.

Yu, Y., Liz Alexander, M., Perraud, V., Bruns, E. A., Johnson, S. N., Ezell, M. J., and Finlayson-Pitts, B. J.: Contamination from electrically conductive silicone tubing during aerosol chemical analysis, Atmos Environ, 43, 2836–2839, https://doi.org/https://doi.org/10.1016/j.atmosenv.2009.02.014, 2009.

Ziemann, P. J. and Atkinson, R.: Kinetics, products, and mechanisms of secondary organic aerosol formation, Chem Soc Rev, 41, 6582, https://doi.org/10.1039/c2cs35122f, 2012.

Table S1. Summary of literature D_5 + OH rate coefficients and measurement methods. We used the empirical values to calculate the average k_{D5+OH}. GC-FID: gas chromatography-flame ionization detector. GC-MS: gas chromatography-mass spectrometry. CIMS: chemical ionization mass spectrometry.

Reference	Method	k_{D5+OH} at ~298 K ($cm^3\ s^{-1}$)
Atkinson (1991)	CH_3NO_2 + UV in 6400 L Teflon chamber, GC-FID, rate relative to cyclohexane.	1.55×10^{-12}
Safron et al. (2015)	O_3/H_2O + UV in 140 mL quartz chamber, GC-MS, rate relative to cyclohexane.	2.6×10^{-12}
Xiao et al. (2015)	O_3/H_2O + UV in 140 mL quartz chamber, GC-MS, rate relative to trimethylpentane.	2.46×10^{-12}
	Computed with Spartan 10 and Merck Molecular Force Field molecular mechanics.	~~2.90×10^{-12}~~
Kim and Xu (2017)	O_3/H_2O + UV in 134 L SilcoNert-coated stainless steel chamber, GC-MS, rate relative to n-hexane.	1.46×10^{-12}
Alton and Browne (2020)	O_3/H_2O + UV in 1000 L Teflon chamber, CIMS, rate relative to propionic acid/MEK.	2.1×10^{-12}
Average		$\mathbf{2.0 \times 10^{-12}}$

Table S2. Summary of PAM OFR experiment conditions.

Experiment	τ_{res} (sec)	Lamp Voltage	RH (%)	T (°C)	O_3 (ppm)	Irradiance (μW cm^{-2})	Volume mode (nm)	Surface mode (nm)	Aerosol sampling line loss (%)	Particle number concentration (cm^{-3})
1	180	2.4	33.27 ± 0.07	22.44 ± 0.07	2.18 ± 0.02	0.95 ± 0.05	68.5	57.3	8.49	9.17×10^4
2	180	2.4	33.53 ± 0.07	21.09 ± 0.09	2.37 ± 0.02	0.93 ± 0.05	85.1	66.1	6.74	1.21×10^5
3	180	2.4	32.45 ± 0.03	19.84 ± 0.16	2.29 ± 0.03	0.83 ± 0.08	82	66.1	6.96	1.34×10^5
4	180	2.4	82.47 ± 0.20	20.39 ± 0.12	1.80 ± 0.02	0.56 ± 0.05	98.2	79.1	5.82	3.24×10^5
5	180	2.4	81.96 ± 0.11	21.37 ± 0.08	1.98 ± 0.03	0.84 ± 0.08	131	101.8	4.33	3.83×10^5
6	180	2.4	82.34 ± 0.11	21.57 ± 0.06	1.82 ± 0.02	0.61 ± 0.03	151.2	121.9	3.80	3.83×10^5
7	180	8.0	28.67 ± 0.30	21.66 ± 0.22	12.62 ± 0.15	12.36 ± 0.11	88.2	71	6.52	1.60×10^5
8	180	8.0	28.82 ± 0.16	21.63 ± 0.22	10.65 ± 0.12	9.37 ± 0.11	140.7	113.4	4.02	1.84×10^5
9	180	8.0	28.58 ± 0.17	23.08 ± 0.19	11.04 ± 0.05	9.80 ± 0.07	187.7	145.9	3.15	2.14×10^5

10	180	8.0	75.62 ± 0.51	21.61 ± 0.29	8.88 ± 0.08	12.18 ± 0.08	121.9	101.8	4.67	4.62×10^5
11	180	8.0	74.91 ± 0.33	23.03 ± 0.18	8.00 ± 0.06	9.68 ± 0.06	151.2	117.6	3.80	5.18×10^5
12	180	8.0	75.64 ± 0.34	23.40 ± 0.20	8.03 ± 0.04	9.67 ± 0.10	194.6	151.2	3.04	6.64×10^5
13	120	2.4	30.57 ± 0.13	20.15 ± 0.14	1.69 ± 0.01	0.87 ± 0.03	51.4	42.9	11.7	6.30×10^4
14	120	2.4	28.97 ± 0.07	21.16 ± 0.08	1.62 ± 0.01	0.84 ± 0.06	55.2	47.8	10.7	5.56×10^4
15	120	2.4	28.48 ± 0.05	21.10 ± 0.06	1.54 ± 0.01	0.69 ± 0.05	57.3	49.6	10.4	4.39×10^4

Table S3. Summary of experiment condensational sinks, LVOC condensation lifetimes, and growth factors calculated with the particle size distribution exiting the PAM-OFR as described in Section S1.3.

Parameters	**SOA, LVOC** κ **= 0.13,** M **= 0.200 kg mol**$^{-1}$			**SOSiA, D_5** κ **= 0.01,** M **= 0.370 kg mol**$^{-1}$		
Experiment	**CS (m^{-2})**	**τ_{CS} (s)**	**Growth Factor**	**CS (m^{-2})**	**τ_{CS} (s)**	**Growth Factor**
1	18237	0.62335	1.0212	13283	0.85585	1.0017
2	28655	0.39672	1.0214	20968	0.54217	1.0017
3	27584	0.41214	1.0204	20183	0.56327	1.0016
4	126160	0.090109	1.1724	73844	0.15395	1.0154
5	221320	0.051365	1.1673	132820	0.085589	1.0149
6	284510	0.039958	1.1711	172260	0.065996	1.0153
7	48329	0.23523	1.0171	35800	0.31754	1.0013
8	100390	0.11324	1.0173	75748	0.15008	1.0014
9	180880	0.062851	1.0171	138940	0.081818	1.0013
10	240210	0.047326	1.1196	153930	0.073853	1.0102
11	372690	0.030503	1.1155	243900	0.046611	1.0099
12	661010	0.017198	1.1197	437730	0.025971	1.0102
13	8963.6	1.2683	1.0187	6506.9	1.7471	1.0015
14	8894.4	1.2781	1.0174	6483.8	1.7533	1.0014
15	7333.8	1.5501	1.0170	5353.1	2.1237	1.0013

Table S4. Proposed PTR-MS VOP ions and identities. Here, "D" refers to units of $(CH_3)_2SiO$ and "T" to CH_3SiO.

Ion Formula	Ion Unit Mass (*m/z*)	Description
$(HCHO)H^+$	31	Formaldehyde
$(HCOOH)H^+$	47	Formic acid
$(C_9H_{27}O_5Si_5)^+$	355	D_5 (-CH_3) or D_4T-OH (-OH) fragment ion
$(C_8H_{25}O_6Si_5)^+$	357	D_3T_2-$(OH)_2$ (-OH) fragment ion
$(C_{10}H_{30}O_5Si_5)H^+$	371	D_5 dominant isotope
$(C_9H_{28}O_6Si_5)H^+$	373	D_4T-OH dominant isotope or H_2O cluster of *m/z* 355
$(C_8H_{26}O_7Si_5)H^+$	375	D_3T_2-$(OH)_2$ dominant isotope
$(C_9H_{25}O_7Si_5)^+$	385	D_3T_2-OH-OCHO (-OH) fragment ion
$(C_{10}H_{28}O_7Si_5)H^+$	401	D_4T-OCHO dominant isotope

Table S5. Reactions and rate coefficients added to the KinSim OFR mechanism template. The rate coefficients (*k*) have units of cm^3 s^{-1} and s^{-1} for bimolecular and unimolecular reactions respectively. Ziemann and Atkinson (2012) **notes that the rates of RO_2 + RO_2 varies by orders of magnitude depending on the structure of the RO_2 and that the products are uncertain. Here, we assumed that the initial RO_2 from D_5 + OH is analogous to secondary alkyl RO_2.** Alton and Browne (2022) **proposes the majority product of RO_2 + HO_2 is RO. The RO_2 + OH rate is for the propylperoxy radical** (Fittschen, 2019)**. For isomerization, we used a value in the range of calculated 1,5 H-shift rates in alkanes, which can vary by orders of magnitude depending on the molecule's functionalization** (Otkjær et al., 2018)**.**

Reference	**Reaction**	**Products**	***k***
Alton and Browne (2022)	RO_2 + HO_2	RO + O_2 + OH (90 %) ROOH (10 %)	1.7×10^{-11}
Ziemann and Atkinson (2012)	RO_2 + RO_2	ROH + R=O 2RO + O_2 ROOR + O_2	5×10^{-15}
Fittschen (2019)	RO_2 + OH	ROOOH RO + HO_2	1.4×10^{-10}
Alton and Browne (2022)	RO_2 rearrangement	RO + HCHO	8.0×10^{-3}
Otkjær et al. (2018)	RO_2 isomerization	R'O_2	1×10^{-3}
Atkinson et al. (2006)	HCHO + OH	HO_2 + CO	8.5×10^{-12}
Atkinson et al. (2006)	CO + OH	HO_2 + CO_2	1.5×10^{-13}

Table S6. Input UV fluxes (cm^{-2} s^{-1}) for KinSim.

Experiment	$[O_3]$ matched		OH_{exp} matched	
	I_{185}	I_{254}	I_{185}	I_{254}
1	3.441×10^{12}	2.375×10^{13}	3.441×10^{11}	2.375×10^{12}
2	3.741×10^{12}	2.325×10^{13}	3.741×10^{11}	2.325×10^{12}
3	3.615×10^{12}	2.075×10^{13}	3.615×10^{11}	2.075×10^{12}
4	4.038×10^{12}	1.400×10^{13}	4.038×10^{11}	1.400×10^{12}
5	4.442×10^{12}	2.100×10^{13}	4.442×10^{11}	2.100×10^{12}
6	4.083×10^{12}	1.525×10^{13}	4.083×10^{11}	1.525×10^{12}
7	1.992×10^{13}	3.090×10^{14}	1.992×10^{12}	3.090×10^{13}
8	1.681×10^{13}	2.343×10^{14}	1.681×10^{12}	2.343×10^{13}
9	1.743×10^{13}	2.450×10^{14}	1.743×10^{12}	2.450×10^{13}
10	1.992×10^{13}	3.045×10^{14}	1.992×10^{12}	3.045×10^{13}
11	1.795×10^{13}	2.420×10^{14}	1.795×10^{12}	2.420×10^{13}
12	1.801×10^{13}	2.418×10^{14}	1.801×10^{12}	2.418×10^{13}
13	5.534×10^{12}	2.175×10^{13}	5.534×10^{11}	2.175×10^{12}
14	5.304×10^{12}	2.100×10^{13}	5.304×10^{11}	2.100×10^{12}
15	5.042×10^{12}	1.725×10^{13}	5.042×10^{11}	1.725×10^{12}

Table S7. Fit first generation relative molar yield (γ_i) and $k_{VOPi+OH}$ of proposed VOP identities. Here, "D" refers to units of $(CH_3)_2SiO$ and "T" to CH_3SiO.

Proposed VOP	γ_i	$k_{VOPi+OH}$ ($cm^3\ s^{-1}$)
D_4T-OCHO (*m/z* 401)	0.0514	4.57×10^{-12}
D_3T_2-OH-OCHO (*m/z* 385)	0.518	5.26×10^{-12}
D_3T_2-$(OH)_2$ (*m/z* 357)	0.343	5.73×10^{-12}
D_4T-OH (*m/z* 355)	1.11	7.53×10^{-12}

Table S8. Experimental molar yields of HCHO and HCOOH. As these species are formed in the OFR at an unknown point, there may be some loss through oxidation with OH. Consequently, the OH_{exp} determined with D_5 may not represent the OH_{exp} these VOP experienced.

Experiment	ΔHCHO/ΔD_5 (ppb/ppb)	ΔHCOOH/ΔD_5 (ppb/ppb)
1	1.79 ± 0.55	0.94 ± 0.15
2	1.35 ± 0.29	0.69 ± 0.09
3	1.21 ± 0.28	0.52 ± 0.09
4	1.52 ± 0.28	0.90 ± 0.09
5	1.28 ± 0.23	0.83 ± 0.09
6	0.96 ± 0.13	0.62 ± 0.05
7	1.06 ± 0.21	0.68 ± 0.05
8	1.18 ± 0.18	0.80 ± 0.07
9	0.88 ± 0.09	0.60 ± 0.04
10	0.69 ± 0.28	1.27 ± 0.11
11	0.55 ± 0.17	0.84 ± 0.06
12	0.52 ± 0.10	0.68 ± 0.04
13	2.11 ± 1.18	0.98 ± 0.37
14	1.11 ± 0.43	0.49 ± 0.12
15	1.15 ± 0.37	0.45 ± 0.12

Table S9. Summary of low-NO$_x$ SOSiA experiments in the literature. The Y_{SOSiA} and C_{OA} from the literature were multiplied by 1.07/(ρ_{SOSiA} used in the reference) to compare with the values from this study. Wu and Johnston (2017) **did not provide a ρ_{SOSiA} nor an OH$_{exp}$, and so we assumed their ρ_{SOSiA} to be the same used here (ρ_{SOSiA} = 1.07 g cm^{-3}) and calculated OH$_{exp}$ using their estimated [OH] and residence time. Moreover, we converted the ΔD$_5$ they report from ppb to μg m^{-3} with 370.8 g mol^{-1}, 298 K, and 1 atm to calculate their Y_{SOSiA}.** Janechek et al. (2019) **conducted experiments with and without ammonium sulfate (AS) seed and found that the SOSiA mass concentration would increase with the addition of seed aerosol. However,** Janechek et al. (2019) **do not explicitly state whether the Y_{SOSiA} in their Table 1 is from those seeded cases.** Charan et al. (2022) **does not provide a summary of C_{OA}, so we calculated them using the values in their Table 1 at 1 atm, and we included the Y_{SOSiA} from their oxidation flow tube with and without the particle wall loss corrections.** Han et al. (2022) **provided a range of ρ_{SOSiA} of 1.6-1.8 g cm^{-3} for a variety of cyclosiloxane precursors, and we used a value of 1.7 g cm^{-3} for the ρ_{SOSiA} adjustment.**

Reference	Experiment Set Up	Y_{SOSiA} (%)	OH$_{exp}$ (s cm^{-3})	C_{OA} (μg m^{-3})	Seed	ρ_{SOSiA} (g cm^{-3})
Wu and Johnston (2017)	PFA photo-oxidation chamber (50 L, τ_{res} = 15 min)	7.9	9×10^{10}	1.2	None	N/A, assumed to be the same used here.
		9.9	9×10^{10}	3.3	None	
		12.7	9×10^{10}	5.6	None	
		14.3	9×10^{10}	8.0	None	
		15.8	9×10^{10}	12.0	None	
		13.8	9×10^{10}	2.3	AS	
		15.1	9×10^{10}	3.2	AS	
		17.5	9×10^{10}	4.5	AS	
		21.8	9×10^{10}	9.6	AS	
		23.1	9×10^{10}	12.6	AS	
Janechek et al. (2019)	PAM-OFR (13.3 L, τ_{res} = 2.7 or 3.8 min)	30	4.8×10^{12}	219.7	N/A	0.959
		24	2.3×10^{12}	84.0	N/A	
		22	1.6×10^{12}	107.1	N/A	
		50	5.1×10^{12}	180.7	N/A	
		24	2.7×10^{12}	68.4	N/A	
Charan et al. (2022)	FEP chamber (19 m^3)	1.5	9×10^{10}	20.	AS	1.52
		5.7	8×10^{10}	44.	AS	
		0	6×10^{10}	0	AS	
		2.6	3×10^{10}	19.	AS	
Charan et al. (2022)	Caltech photo-oxidation flow tube (τ_{res} = 671 s)	1.9/1.1	1.4×10^{10}	1.3	None	1.52
		2.9/1.8	1.5×10^{11}	19	None	
		9.2/6.0	3.3×10^{11}	67	None	
		6.7/4.6	1.5×10^{11}	70.	None	
		19/14	7.8×10^{11}	336	None	
		32/24	1.0×10^{12}	643	None	

		49/35	1.1×10^{12}	993	None	
		157/109	3.2×10^{12}	3969	None	
		158/110	3.2×10^{12}	4046	None	
		138/102	3.1×10^{12}	1276	None	
		128/94	3.3×10^{12}	1176	None	
Han et al. (2022)	Environment and Climate Change Canada OFR (16 L, τ_{res} = 2 min)	2	5.5×10^{10}	0.5	None	1.6-1.8
		2	1.4×10^{11}	1.8	None	
		11	3.5×10^{11}	16.9	None	
		27	5.0×10^{11}	48.9	None	
		35	6.0×10^{11}	68.7	None	
		46	6.9×10^{11}	97.7	None	
		61	9.0×10^{11}	169.7	None	
		70	1.2×10^{12}	228.8	None	
		75	1.3×10^{12}	253.6	None	
		79	1.7×10^{12}	282.7	None	
		80	1.9×10^{12}	273.6	None	
		2	5.5×10^{12}	0.8	AS	
		1	1.4×10^{12}	2.0	AS	
Avery et al. (2023)	PAM-OFR (13.3 L, τ_{res} = 130 s)	2	1.15×10^{12}	3.84	None	1.78
		16	2.42×10^{12}	28.47	None	1.67
		37	3.77×10^{12}	66.89	None	1.64
		42	4.55×10^{12}	76.12	None	1.61
		82	5.23×10^{12}	149.44	None	1.60
		104	6.21×10^{12}	189.02	None	1.60
		146	8.23×10^{12}	267.47	None	1.59

Table S10. Odum 2-product model fit values. These 2-product parameterizations do not account for OH_{exp}. Janechek et al. (2019) **and** Charan et al. (2022) **state the values below, and** Charan et al. (2022) **provided 2 fits: with/without particle wall-loss corrections.** Han et al. (2022) **and** Avery et al. (2023) **did not provide 2-product parameterizations, so we fit their data that was adjusted to ρ_{SOSiA} = 1.07 g cm^{-3}; the original ρ_{SOSiA} are in Table S9. We also performed a fit with all values, including those in the literature.**

Reference	α_1	α_2	K_1	K_2
Janechek et al. (2019) (ρ_{SOSiA} = 0.959 g cm^{-3})	0.14	0.82	1.05	0.00207
Charan et al. (2022) (ρ_{SOSiA} = 1.52 g cm^{-3})	0.056/0.044	7.7/5.5	0.022/0.027	4.3×10^{-5}/6.0×10^{-5}
Han et al. (2022) (ρ_{SOSiA} = 1.07 g cm^{-3})	0.4598	1.284	1.432×10^{-2}	8.546×10^{-4}
Avery et al. (2023) (ρ_{SOSiA} = 1.07 g cm^{-3})	5.301	9.756	3.161×10^{-4}	4.209×10^{-4}
This paper (ρ_{SOSiA} = 1.07 g cm^{-3})	0.2266	0.6864	0.01478	9.611×10^{-4}
All Values (ρ_{SOSiA} = 1.07 g cm^{-3})	0.3774	1.743	0.02482	2.486×10^{-4}

Table S11. Fit VBS product mass yields (α_i) and chemical aging rate coefficients ($k_{age,gas}$). The $k_{age,gas}$ is for the aging-VBS model where OH_{exp} is explicitly parameterized with the and "bin-hopping" as described in Section 3.2. We performed fits using the data from our experiments and all values, which includes those in the literature. For α_i smaller than 10^{-5}, we marked them as 0.

C*	**0.1**	**1**	**10**	**100**	**1000**	**10000**	$k_{age,gas}$
This study α_i (no aging)	8.467×10^{-4}	0	0.1193	0	0.7043	0.1756	N/A
This study α_i (aging)	1.237×10^{-4}	2.320×10^{-3}	1.373×10^{-2}	8.674×10^{-2}	2.913×10^{-5}	0.8971	2.169×10^{-11}
All values α_i (no aging)	7.412×10^{-2}	0	0	0	0.6599	0.2660	N/A
All values α_i (aging)	8.328×10^{-5}	1.562×10^{-3}	9.242×10^{-3}	5.839×10^{-2}	2.319×10^{-5}	0.9307	1.086×10^{-11}

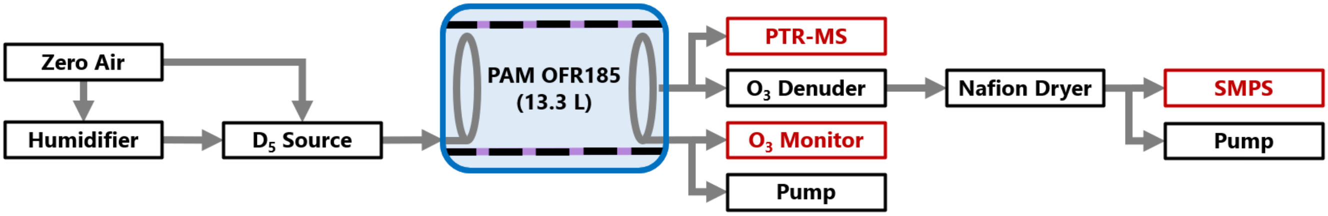

Figure S1. PAM-OFR experiment set up. The D_5 source was a syringe pump injecting into a passivated glass bulb. The side ports were equipped with conductive Teflon flow rings on both ends of the PAM-OFR. We covered 90 % of the 185 nm UV lamps to achieve lower irradiances and OH_{exp}. We conducted experiments at τ_{res} = 120 s with 6.65 L min^{-1} or 180 s with 4.43 L min^{-1} respectively.

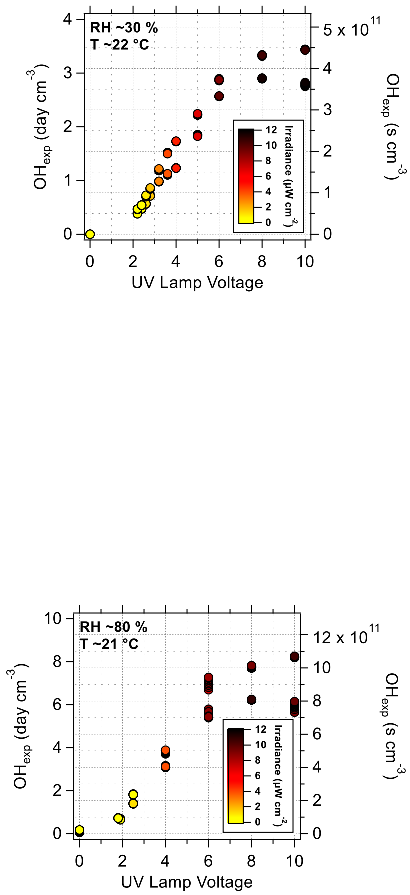

Figure S2. Offline OH$_{exp}$ calibrations with CO at low and high humidity conditions. The OH$_{exp}$ measured during experiments with D$_5$ were consistent with the offline calibration values.

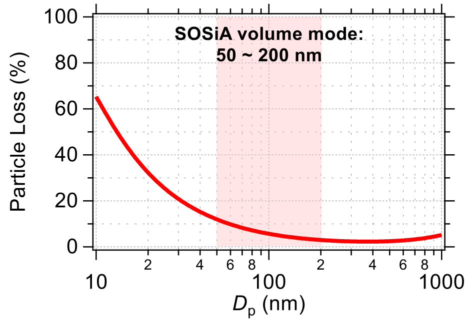

Figure S3. Calculated particle losses with diameters (von der Weiden et al., 2009) **using the dimensions of the aerosol sampling line. The shaded area refers to the aerosol volume modes found during experiments.**

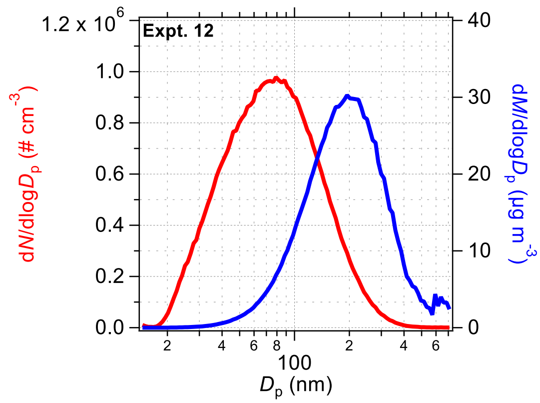

Figure S4. SOSiA particle size distribution for experiment 12, where $[D_5]_0$ and OH_{exp} were high.

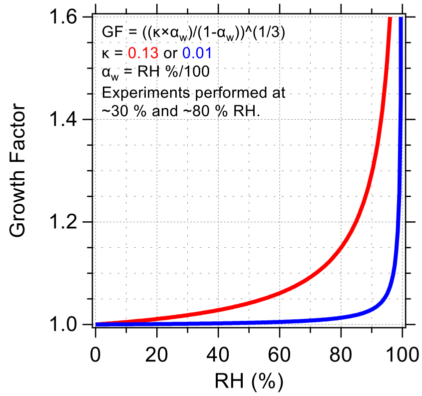

Figure S5. Particle growth factor vs. RH (%) for *κ* = 0.13 and 0.01. Palm et al. (2016) **used the SOA hygroscopicity factor (*κ* = 0.13), while** Janechek et al. (2019) **found SOSiA to be non-hygroscopic (*κ* = 0.01).**

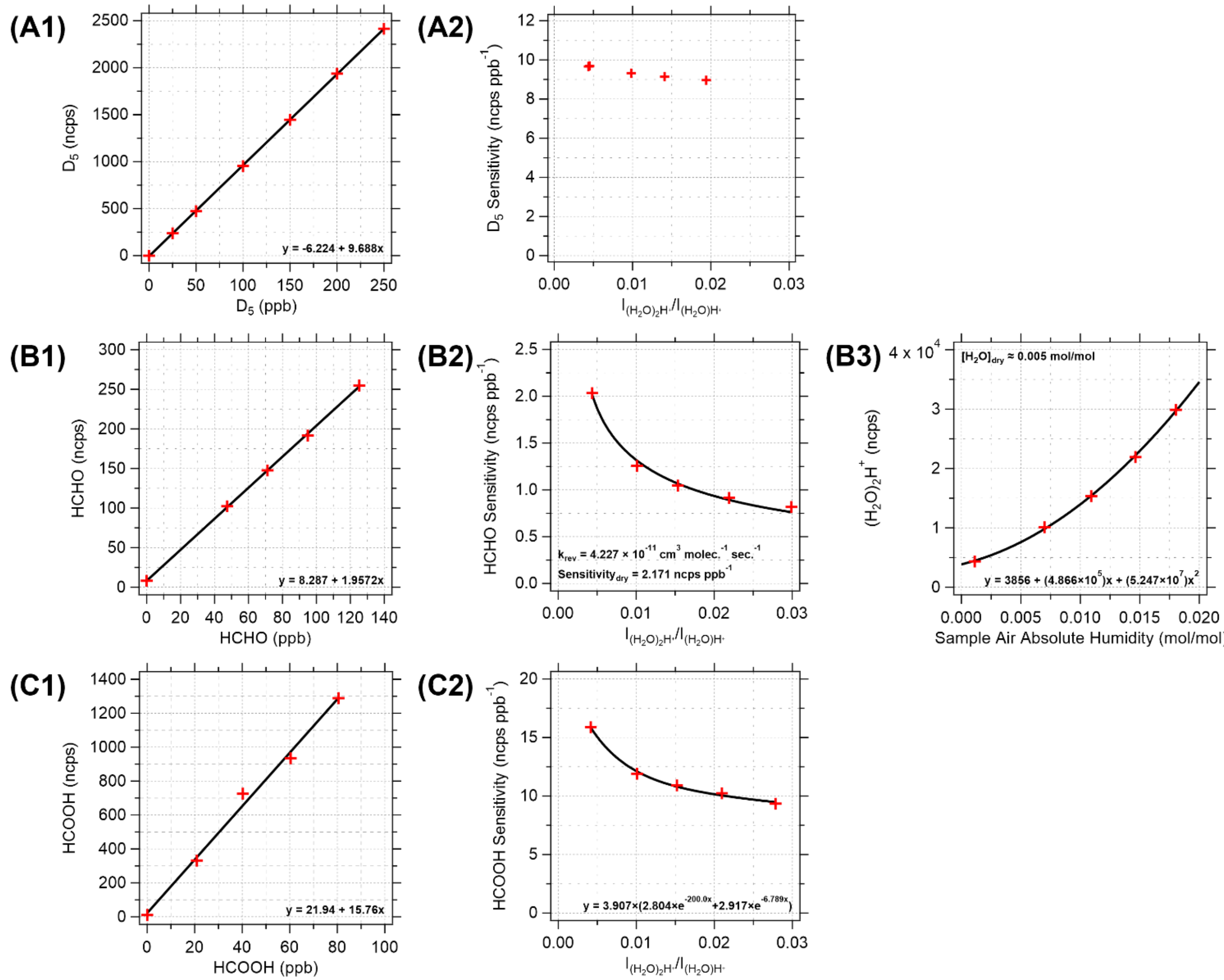

Figure S6. (A1, B1, C1) Calibration curves of D_5, HCHO, and HCOOH. The PTR-MS response was linear under these concentration ranges. (A2, B2, C2) Sensitivity variation with humidity. We found the D_5 sensitivity at *m/z* 371 under 137 Td to be consistent with changing humidity and did not apply a correction for the quantification. (B3) Polynomial fit to determine the H_2O mixing ratio contribution from the PTR-MS ion source.

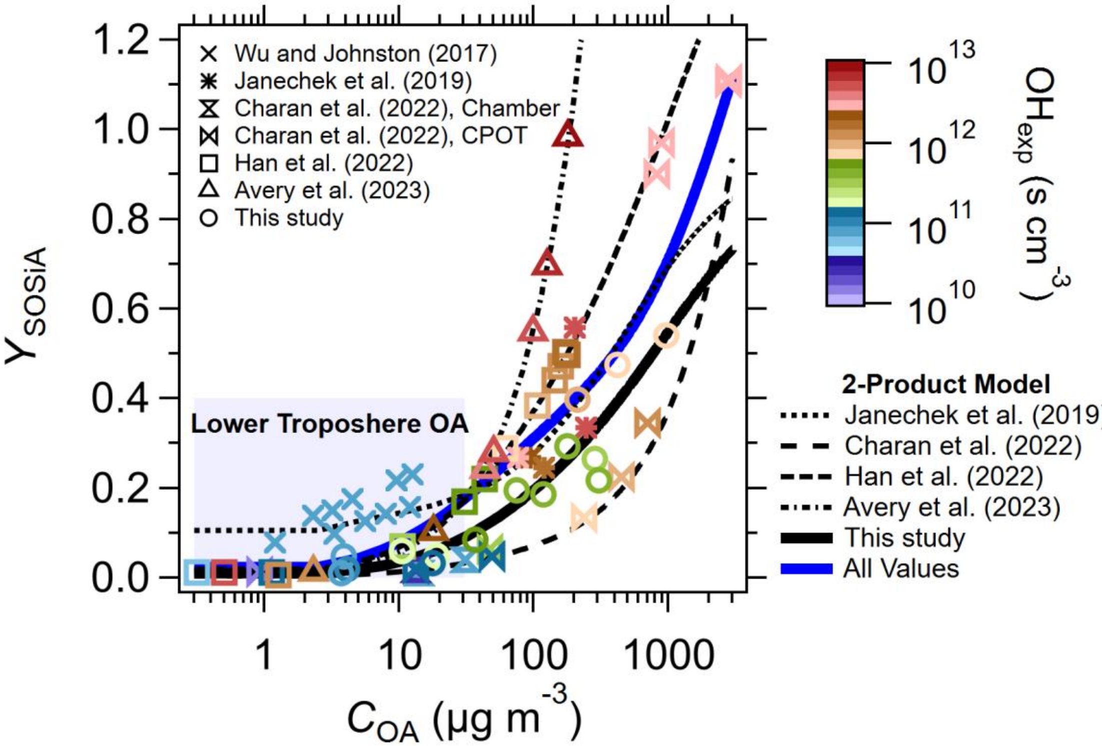

Figure S7 Comparison of Odum 2-product model parameterizations between this study and the literature. The blue line is from the fit with all data, including those we report. The shaded area indicates the range of ambient OA concentrations commonly observed in the lower troposphere (Porter et al., 2021). The figure shows the particle wall loss-corrected values from Charan et al. (2022). Han et al. (2022) and Avery et al. (2023) did not provide 2-product parameterizations, so we fitted the values using their ρ_{SOSiA}-adjusted data (Table S10). Wu and Johnston (2017) did not have measurements of OH_{exp} or D_5 and instead provided estimates. The OH_{exp} (color scale) are those reported by the literature.

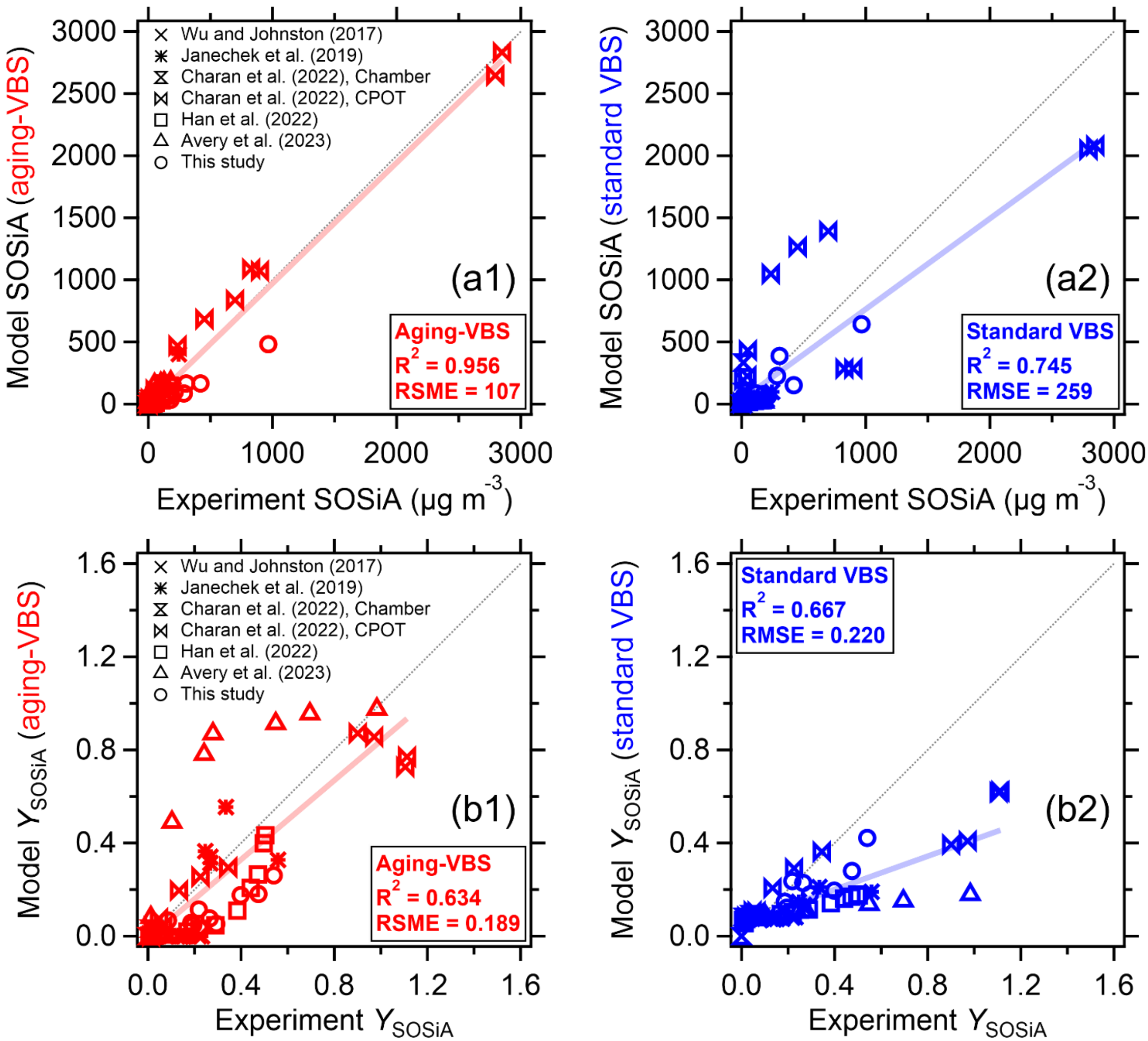

Figure S8. Comparison of the (a) SOSiA mass and (b) Y_{SOSiA} from the (1) aging-VBS and (2) standard-VBS parameterizations fit with values we report and those in the literature (Table S11). The R^2 and root mean square error (RMSE) of the aging-VBS model SOSiA is better than that of the standard VBS.

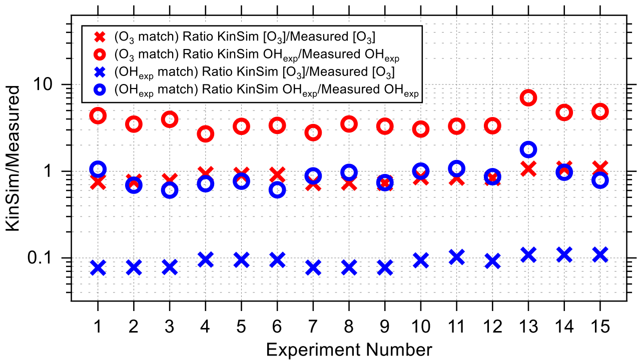

Figure S9. Ratio of the KinSim model outputs vs. measurements for each experiment. The "OH_{exp} match" and "O_3 match" refers to the cases where the UV flux is and is not adjusted so that the KinSim outputs of OH_{exp} and O_3 are in line with measurements respectively.

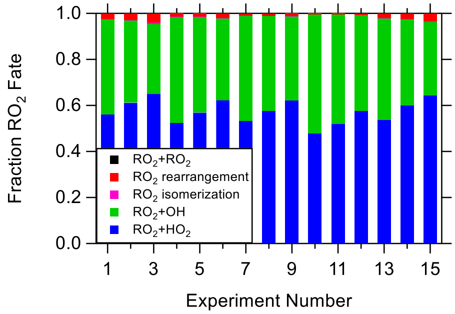

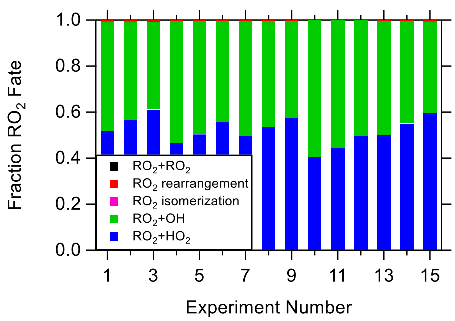

Figure S10. KinSim estimations of RO_2 fates across experiments. The top panel has I_{254} and I_{185} multiplied by 0.1 (OH_{exp} matched), while the bottom does not (O_3 matched). In either case, KinSim calculated the RO_2 fates in all experiments to be dominated by the RO_2 + HO_2 and RO_2 + OH pathways.